

PIM-1 as a Multifunctional Framework to Enable High-Performance Solid-State Lithium–Sulfur Batteries

Yuchen Ji, Kai Yang, Mingqiang Liu, Shiming Chen, Xinhua Liu,* Biao Yang, Zijian Wang, Weiyuan Huang, Zhibo Song, Shida Xue, Yanda Fu, Luyi Yang,* Thomas S. Miller, and Feng Pan*

Poly(ethylene oxide) (PEO) is a promising solid electrolyte material for solid-state lithium–sulfur (Li–S) batteries, but low intrinsic ionic conductivity, poor mechanical properties, and failure to hinder the polysulfide shuttle effect limits its application. Herein, a polymer of intrinsic microporosity (PIM) is synthesized and applied as an organic framework to comprehensively enhance the performance of PEO by forming a composite electrolyte (PEO-PIM). The unique structure of PIM-1 not only enhances the mechanical strength and hardness over the PEO electrolyte by an order of magnitude, increasing stability toward the metallic lithium anode but also increases its ionic conductivity by lowering the degree of crystallinity. Furthermore, the PIM-1 is shown to effectively trap lithium polysulfide species to mitigate against the detrimental polysulfide shuttle effect, as electrophilic 1,4-dicyanooxanthrene functional groups possess higher binding energy to polysulfides. Benefiting from these properties, the use of PEO-PIM composite electrolyte has achieved greatly improved rate performance, long-cycling stability, and excellent safety features for solid-state Li–S batteries. This methodology offers a new direction for the optimization of solid polymer electrolytes.

1. Introduction

With the technological development of electric vehicles, grid-scale energy storage and portable electronic equipment, the demand for the advanced batteries with high performance has

continuously increased dramatically in the last few decades.^[1–3] Lithium–sulfur (Li–S) batteries have attracted much attention because of their high theoretical energy density (2600 Wh kg⁻¹),^[4] low cost, and the high earth-abundance of sulfur.^[5] However, although the use of a metallic Li anode in Li–S batteries is significantly safer than in a lithium ion battery, the formation of Li dendrites can still lead to the short circuiting of cells, with the consequent safety issues.^[6] Developing solid-state Li–S batteries without flammable liquid organic electrolytes is a promising route to overcome these challenges.^[6–10]

Among the various solid-state electrolytes available, poly(ethylene oxide) (PEO) has been extensively researched due to its merits of good film-forming ability, flexibility, and low interfacial resistance.^[11,12] However, the intrinsic shortcoming of low ionic conductivity (10^{-6} – 10^{-7} S cm⁻¹ at room temperature) limits its application in commercially relevant batteries; the semi-crystalline nature of the PEO matrix hinders the formation of continuous Li⁺ transfer pathways.^[13] In addition, the mechanical strength and hardness of PEO electrolytes are not high enough to resist lithium dendrite growth, allowing short circuits at relatively low current densities.^[14] Moreover, having a similar molecular structure to polyether liquid electrolytes (e.g., dimethoxyethane), PEO can also dissolve lithium polysulfides and allow the polysulfide shuttle effect to occur, a significant driver in Li–S battery degradation.^[15] Consequently, PEO-based solid-state Li–S batteries generally suffer from rapid capacity decay and low Coulombic efficiencies, especially when operated at temperatures approaching the melting temperature of PEO (\approx 60 °C).^[16]

Many strategies have been suggested to improve the overall performance of PEO-based electrolytes in solid-state Li-ion batteries, such as creating composite solid electrolytes,^[17] optimization of lithium salts,^[18–20] incorporation of ceramic or inorganic nanoparticles as fillers,^[21,22] and the introduction of novel polymer composites,^[23,24] or quasi-ionic liquids,^[25] into the electrolyte.^[25] Unfortunately, few strategies manage to mitigate the shuttling of polysulfides within the PEO polymer, or eliminate dendrites, limiting the effectiveness of these solid polymer electrolytes (SPEs) in solid-state Li–S batteries.

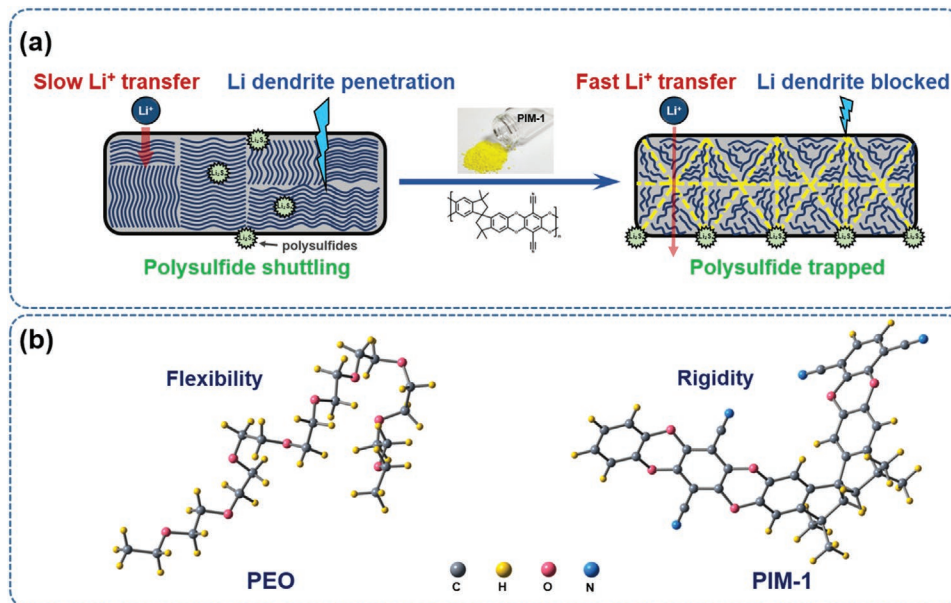
Polymers of intrinsic microporosity (PIMs) are a class of microporous polymer material with rigid and contorted

Y. Ji, K. Yang, M. Liu, S. Chen, B. Yang, Z. Wang, W. Huang, Z. Song,
S. Xue, Y. Fu, L. Yang, F. Pan
School of Advanced Materials
Peking University Shenzhen Graduate School
Shenzhen 518055, P. R. China
E-mail: yangly@pkusz.edu.cn; panfeng@pkusz.edu.cn

M. Liu, T. S. Miller
Electrochemical Innovation Lab
University College London
London WC1E 7JE, UK
M. Liu, T. S. Miller
The Faraday Institution
Quad One, Becquerel Avenue, Harwell Campus, Didcot OX11 ORA, UK
X. Liu
School of Transportation Science and Engineering
Beihang University
Beijing 100191, China
E-mail: liuxinhua19@buaa.edu.cn

 The ORCID identification number(s) for the author(s) of this article can be found under <https://doi.org/10.1002/adfm.202104830>.

DOI: 10.1002/adfm.202104830



Scheme 1. a) Schematic illustration of how PIM-1 boosts the performance of PEO-based solid-state Li-S batteries. b) 3D molecular structures and properties of PEO and PIM-1.

spiro-centers in their backbone, preventing an efficient packing of the consistent macromolecules in the solid state.^[26] The presence of abundant, stable, and interconnected micropores mean PIMs are widely applied in gas adsorption,^[27] separation,^[28,29] and electronic devices.^[30] They also offer both rigidity and flexibility, as they are organic materials with rigid chains.^[31] Nonetheless, their application in the field of energy storage has seldom been reported.

In this work we couple the multifaceted structural and mechanical properties of PIMs^[31] with the proven ability of PEO-based Li-S battery electrolytes to form a solid polymer electrolyte (SPE) with both high conductivity and resistance to traditional degradation mechanisms. PIM-1 (a first generation PIM, Scheme S1, Supporting Information) is utilized as a framework into which a PEO electrolyte is inserted to form a composite solid electrolyte, effectively enhancing the mechanical strength of the PEO. This SPE is shown to resist lithium dendrite growth, and the built-in framework decreases the degree of crystallinity of the PEO, increasing the lithium ion conductivity. Moreover, the electrophilic 1,4-dicyanooxanthrene functional groups in PIM-1 effectively trap polysulfides, due to their high binding energy, hence retarding the shuttling effect of polysulfides. As shown in **Scheme 1**, together these features produce solid-state Li-S batteries with a PEO-PIM composite electrolyte that exhibit outstanding rate performance and cycling stability.

2. Result and Discussion

The composite solid electrolytes were obtained by separately dissolving PIM-1 in trichloromethane and PEO in acetonitrile (CH_3CN), and then mixing the two to obtain a homogenous solution, which was subsequently cast on a Teflon substrate and dried, forming smooth and flat films (see methods for more details). As shown in **Figure 1a**, the prepared PEO-PIM

composite solid electrolyte is a uniform bright yellow translucent membrane without obvious powder agglomerates, the opacity of the PEO-PIM membrane increases with the percentage of PIM-1 (Figure S1, Supporting Information). This free-standing PEO-PIM SPE is flexible and mechanically stable, being resistant to bending without cracking (Figure 1a). Scanning electron microscope (SEM) images show that the surface morphology of PEO-PIM is flat and smooth without phase segregation (Figure S2, Supporting Information). As PIM-1 is known to be good at film-forming (Figure S3, Supporting Information), this suggests that instead of being distributed independently, PIM-1 tends to form a (partially) connected network within the composite electrode.

It is well known that the mechanical properties of SPEs are critical to the overall performance of solid-state batteries: high mechanical strength is essential to resist lithium dendrite growth and withstand stress.^[32] The tensile strength of the as-prepared solid electrolytes with different ratios of PIM-1 were assessed by stress-strain curves (Figure 1b). The elastic limit of PEO-PIM electrolyte reaches 0.5, 0.9, and 1.3 MPa as the weight percentage of PIM-1 increases to 4%, 8%, and 12%, respectively (inset, Figure 1b), a significant improvement compared to that of pure PEO (0.3 MPa). The high elastic limit reveals that PEO-PIM electrolytes could better resist elastic deformation under the influence of the external environment. It is noteworthy that PEO-PIM (8%) exhibits the highest elongation strain limit (2000%), which infers that an excess amount of PIM-1 may compromise elasticity. Next, in order to simulate the growth process of lithium dendrites in solid-state batteries, nano-indentation was employed to measure the compressive strength of PEO and PEO-PIM (Figure 1c).^[33] Both PEO and PEO-PIM are compressed to the same depth and the force feedback was measured synchronously. The force feedback of PEO-PIM become larger with the increase of PIM-1 content (0.8 mN, 4%; 1.5 mN, 8%; 2.2 mN, 12%), and the results are an

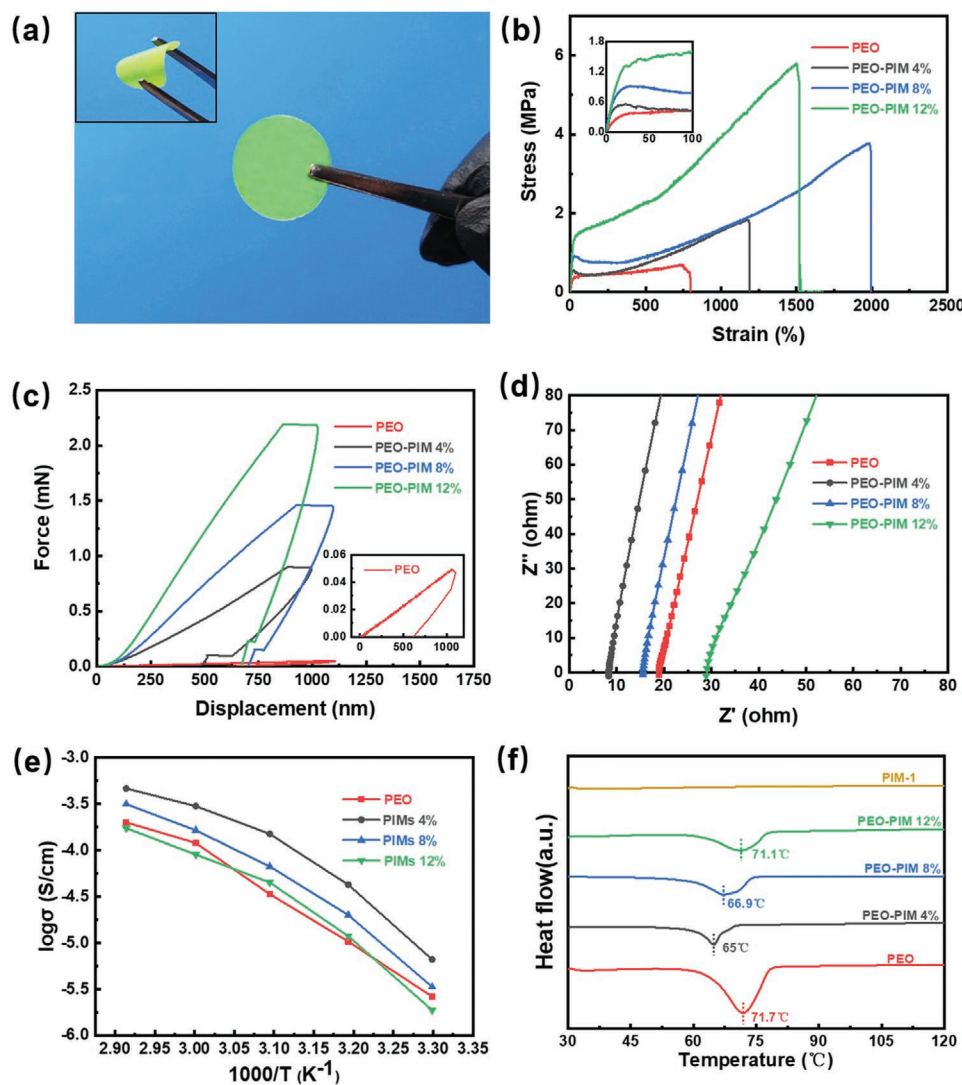


Figure 1. a) Optical photographs of prepared PEO-PIM membranes. b) Stress–strain curves of PEO and PEO-PIM (4%, 8%, and 12%) under tensile test. c) Load–displacement curves of PEO and PEO-PIM (4%, 8%, and 12%) under nano-indentation test. d) EIS curves of PEO and PEO-PIM (4%, 8%, and 12%) at working temperature (60 °C). e) Ionic conductivities of PEO and PEO-PIM (4%, 8%, and 12%). f) DSC profiles of PIM-1 material, PEO, and PEO-PIM (4%, 8%, and 12%) membrane in the absence of Li salt.

order of magnitude higher than those for PEO (0.05 mN), thus the introduction of PIM-1 significantly improves the compressive strength.

Next, the ionic conductivity of SPEs from 30 to 70 °C was measured by electrochemical impedance spectroscopy (EIS). The Nyquist (Figure 1d) and Arrhenius (Figure 1e) plots of PEO and PEO-PIM electrolytes show that as the ratio of PIM-1 increases, the conductivity of the SPEs initially increases, up to a maximum at 4%, then decreases (see detailed data in Figure S4, Supporting Information). Above 8% the conductivity is lower than pure PEO. This drop in conductivity is expected due to the low intrinsic conductivity of the PIM, hence excessive PIM-1 in the composite polymer electrolyte will block ion transfer pathways by disrupting the continuity of PEO domains. However, at low percentages, PIM-1 does increase the SPE conductivity. The ionic conductivity of PEO-based SPEs is closely related to its crystallinity.^[21] Low crystallinity improves the chain motility

of PEO, allowing it to rapidly transfer Li⁺ in the interlayer channels.^[24] Additionally, X-ray diffraction patterns of the composite electrolytes (Figure S6, Supporting Information) also infer that PIM-1 has lowered the crystallinity of PEO.

Differential scanning calorimetry (DSC) was carried out to further investigate the mechanism of improved Li-ion conductivity. To exclude the impact of lithium bis(trifluoro-methane-sulfonyl)imide (LiTFSI), composite electrolytes without lithium salt were measured (Figure 1f). The incorporation of PIM-1 can be seen to inhibit the polymer crystallization, leading to a change of melting point from 71.7 to 65 °C (4%), 66.9 °C (8%), and 71.1 °C (12%). The DSC results indicate that the addition of PIM-1 promotes the movement of PEO segments by disrupting the crystalline regions, which resembles the effect of adding nano-fillers into PEO-based electrolytes.^[21] This can be attributed to the strong interaction between PIM-1 and PEO, which weakens the intermolecular interaction between PEO chains,

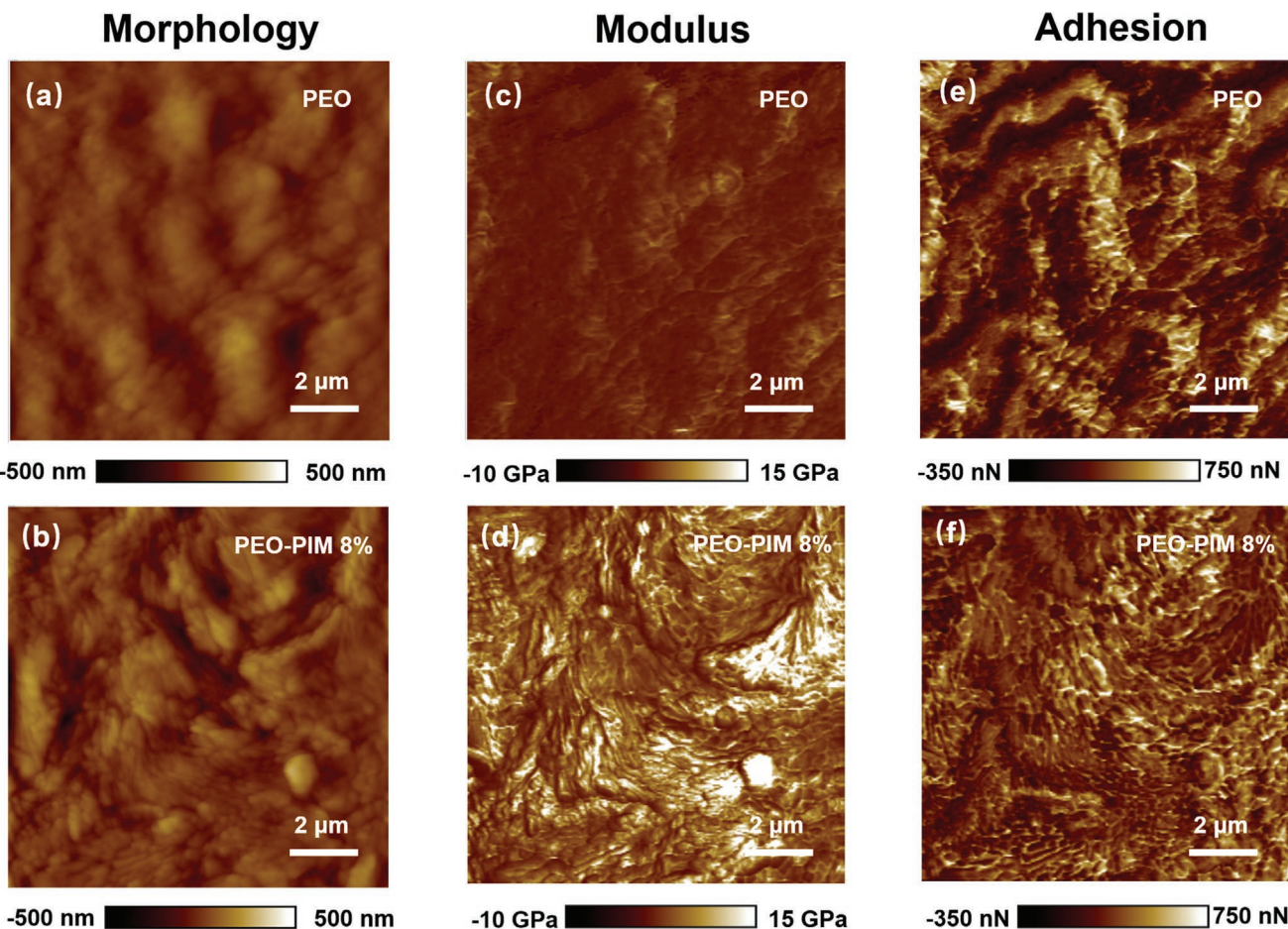


Figure 2. Surface morphology and corresponding mechanical properties of solid polymer electrolytes measured via AFM. a) PEO morphology, b) PEO-PIM morphology, c) PEO modulus distribution, d) PEO-PIM modulus distribution, e) PEO adhesion distribution, and f) PEO-PIM adhesion distribution.

hence the lowering the crystallinity. The DSC results of polymer electrolyte containing lithium salt are presented in Figure S7, Supporting Information. The significant decrease of melting point from 62.1 to 55 °C with the introduction of PIM-1 (8%) indicates that the mechanism of improved Li-ion conductivity discussed above also hold for the SPEs in practical application.

Quantitative nano-mechanics mode atomic force microscope (AFM) was applied to quantitatively reveal the changes in morphology (Figure 2a,b), relative modulus (Figure 2c,d), and adhesion (Figure 2e,f) caused by the addition of 8% PIM-1 to PEO.^[34] Compared with the surface morphology of PEO (Figure 2a), PEO-PIM exhibits a rougher surface (see detailed data in Table S1, Supporting Information) with smaller domains, inferring a lowered crystallinity, which is in accordance with DSC results. Moreover, the average modulus of the PEO-PIM (8%) sample was found to be 8.48 GPa (Figure 2c), significantly higher than that found for PEO alone 0.87 GPa (Figure 2d), confirming that the PIM improves the mechanical strength of the SPE. Interestingly, although it is generally seen that an increase in hardness is accompanied by a decrease of adhesion which leads a poor contacted interface between SPE and electrodes,^[35] the average adhesion force of PEO-PIM membrane (Figure 2e) is even higher than that PEO (213 vs 114 nN, Figure 2f). This could provide further evidence that the addition of rigid PIM-1 not only

forms a hard framework to improve the mechanical strength at the macroscopic level, but also disrupts the crystalline regions of PEO to promote segment movement at the microscopic level. As a result, PEO-PIM inherits not only the rigidity of PIM-1,^[31] meaning it can resist lithium dendrite penetration, but also the flexibility of PEO^[17] to enable good contact with electrodes.

Fourier transform infrared (FT-IR) measurements were applied to investigate the nature of the interactions between PIM-1 and PEO (Figure S8, Supporting Information), and no additional peaks are observed in the spectra after mixing. This suggests that there is no significant chemical bonding between PIM-1 and PEO. It can be speculated that the interactions between PIM-1 and PEO mainly result from the dipole–dipole attraction between 1,4-dicyanooxanthrene functional groups in PIM-1 monomer with the O atoms of the ether groups in the PEO segments.

Although mechanical tests can be indicative of an SPE's resistance against Li dendrites, this must also be proven in situ. The stability of the PEO-PIM electrolyte against penetration of dendrites was tested in symmetric Li/SPE/Li cells via galvanostatic plating and stripping at 60 °C (Figure 3). The symmetric cells using PEO-PIM (8%) demonstrate outstanding stability: at 0.05 mA cm⁻² they present an initial overpotential of 0.015 V and remain operative for over 700 h (Figure S11c, Supporting

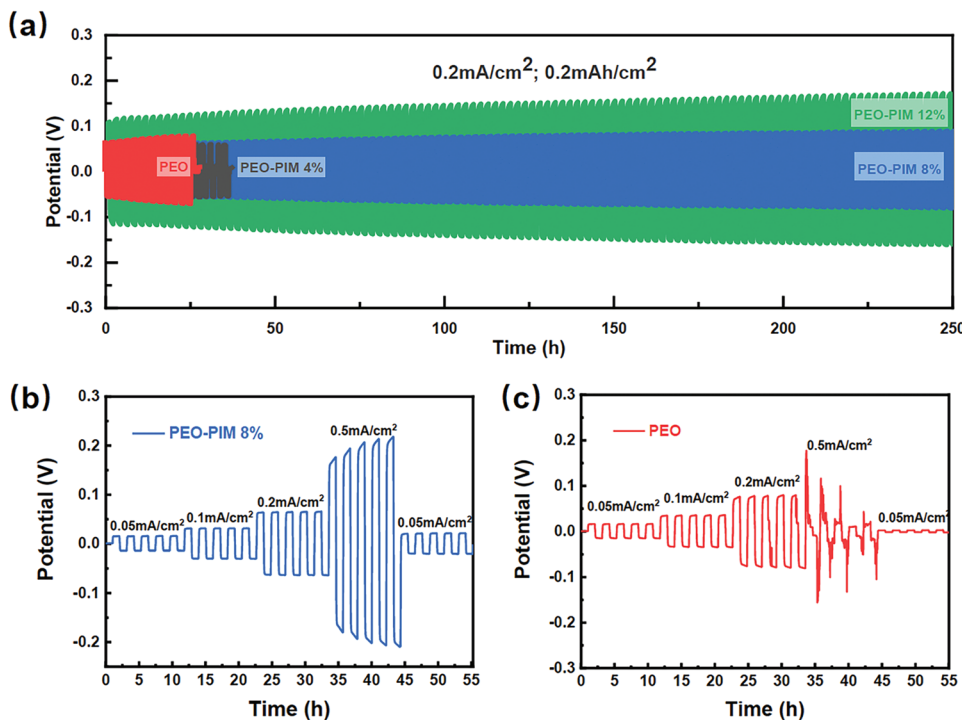


Figure 3. Voltage profiles of Li symmetrical cells of a) PEO and PEO-PIM (4%, 8%, and 12%) at 0.2 mA cm^{-2} . b) PEO-PIM (8%) and c) PEO at different current densities from 0.05 to 0.5 mA cm^{-2} .

Information); at 0.2 mA cm^{-2} the overpotential is 0.055 V and the cells survive for over 250 h (Figure 3a). This is in sharp contrast to the equivalent data for the pure PEO electrolyte, which displays a sudden potential drop after 124 h (0.05 mA cm^{-2}) and 28 h (0.2 mA cm^{-2}) of cycling, due Li dendrites piercing the electrolyte to cause a short circuit.^[36] The overpotential of the PEO electrolyte reached 0.078 V at 0.2 mA cm^{-2} , much higher than that for the PEO-PIM electrolyte. The impact of the PIM-1 ratio in the SPEs on Li plating/stripping performance was also tested. Although the SPE with 4% of PIM-1 has been shown to exhibit the highest ionic conductivity, which is also reflected in the fact it had lowest overpotential (0.01 V at 0.05 mA cm^{-2} and 0.05 V at 0.2 mA cm^{-2}), it appears less able to resist Li dendrite growth as it short-circuited within short periods (Figure S11b, Supporting Information, and Figure 3a). As the ratio increases to 12%, the ionic conductivity becomes too low, leading to the large overpotentials, although the cells did still survive for extended periods (Figure S11d, Supporting Information, and Figure 3a). Operation at higher current densities is also desirable for solid-state batteries, hence the current limit of Li/SPE/Li cells was investigated.^[37] Figure 3b,c demonstrates that PEO-PIM (8%) can function at 0.5 mA cm^{-2} , while sudden failure occurs in the cell with pristine PEO at this current density. The improved critical current density widens the application of PEO-based SPE in Li metal batteries.

It has been previously reported that the 1,4-dicyanooxanthrene functional group in PIM-1 exhibits strong electrophilicity, which is likely to bond with nucleophilic polysulfides.^[26,38] Density functional theory (DFT) simulations were used to identify the probable binding sites (Figure 4a and Figure S12, Supporting Information, taking Li_2S_6 for an example) and binding

energies (Figure 4b and Table S2, Supporting Information) of various polysulfide species ($\text{Li}_2\text{S}_2 \approx \text{Li}_2\text{S}_8$) with PIM-1 and PEO. The DFT results show that the binding energies of PIM-1 to polysulfides are much higher than those of PEO by 60.0–86.4%. Hence, polysulfides are likely to be trapped on the active site of immobile PIM-1 in Li–S cells (according to the DSC results in Figure 1f, melting point of PIM-1 is far beyond $60 \text{ }^\circ\text{C}$), rather than to the ether bonds of PEO, whose chain segments are mobile at this working temperature. This may act to mitigate the shuttling effect and reduce loss of inventory.

To confirm the suppressing effect of PIM-1 on polysulfide shuttling, cathodes consisting of sublimed sulfur without a carbon host (so its impact can be ruled out) were prepared for cell testing at $60 \text{ }^\circ\text{C}$. Cycling performance of cells using PEO and PEO-PIM (4%, 8%, and 12%) SPEs are compared in Figure 4c. The cell with pristine PEO shows rapid failure after a small number of cycles, which is likely, in part, due to the unconstrained polysulfide shuttling. By contrast, the addition of PIM-1 facilitates much improved capacity retention with an optimal ratio of 8%, which outperforms other ratios. It is speculated that an insufficient amount (4%) of PIM-1 cannot effectively block polysulfide shuttling while an excessive amount (12%) could cause the loss of active materials due to the strong binding between polysulfide and PIM-1.

Next, to further investigate the inhibition effect of polysulfide shuttling, S_{2p} X-ray photoelectron spectra of lithium anodes cycled (three cycles) in cells with PEO-PIM (8%) and PEO electrolytes are shown in Figures 4d and 4e, respectively. The characteristic peaks of Li_2S_2 at $161.4 \text{ eV}^{[8]}$ are detected on the anode with PEO and not found for PEO-PIM. In addition, the relative intensity ratio between PS species and $\text{SO}_2/\text{SO}_3^{2-}$ for PEO electrolyte is much

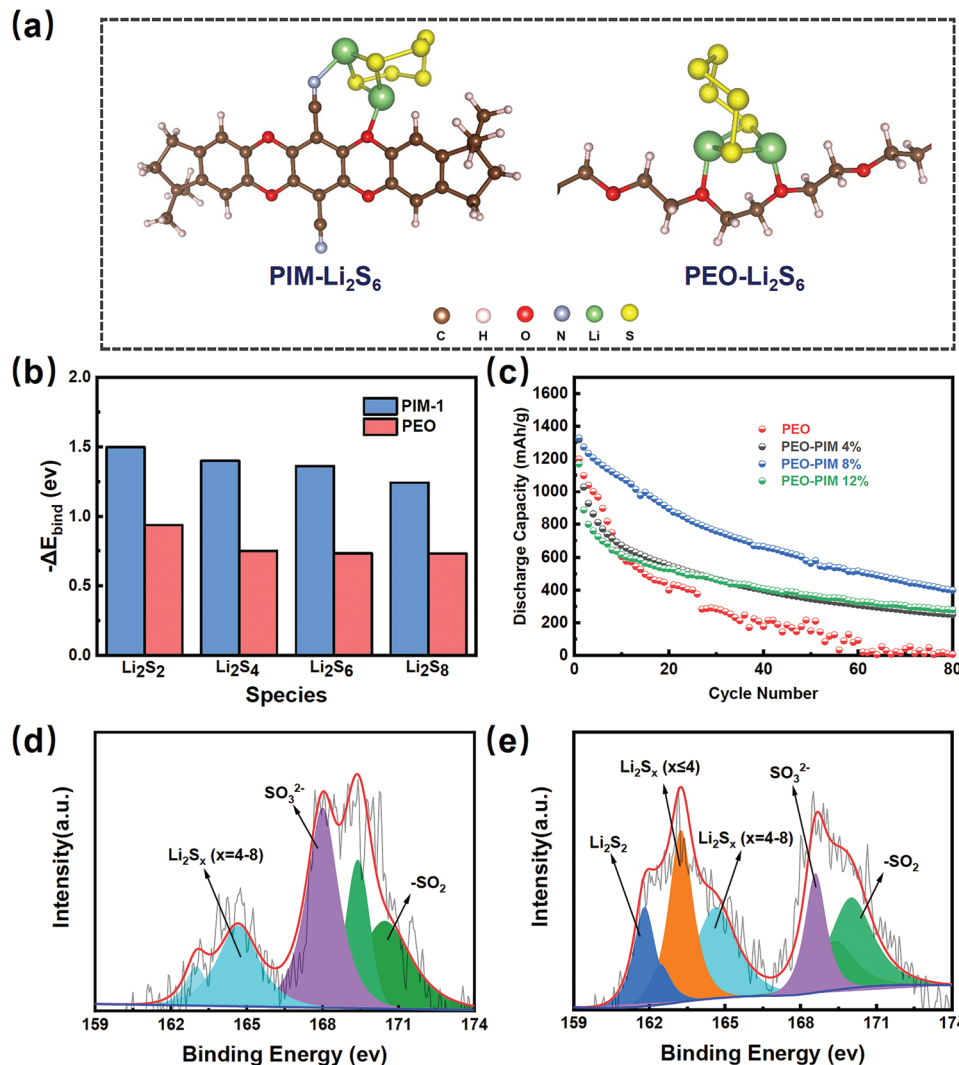


Figure 4. a) Fully optimized structures of the stationary points for Li_2S_6 on PEO and PIM-1. b) DFT calculation results of the corresponding binding energies of various polysulfides (Li_2S_2 - Li_2S_8) with PEO and PIM, respectively. c) Cycling performance of S/PEO/Li cells and S/PEO-PIM/Li (4%, 8%, and 12%) in the absence of hosting materials for sulfur under 0.05C at 60 °C. XPS S_{2p} spectra of lithium electrode obtained from d) S/PEO-PIM/Li and e) S/PEO/Li cells after three cycles.

higher than PEO-PIM, revealing that PEO caused much severe polysulfide dissolution compared with PEO-PIM electrolyte.

Full cells consisting of a sulfur–carbon composite cathode, a Li metal anode, and the PEO-based SPEs were assembled and tested to assess the SPEs in an industrially relevant configuration at 60 °C. Since the PIM-1 (8%) material exhibited the best overall performance, this ratio was used for the PEO-PIM full cell tests. Rate performance is first evaluated. As shown in Figure 5a, the battery capacity of PEO-PIM-8% at 0.1C remains much more stable (only 135 mA h g⁻¹ capacity decay) than PEO (503 mA h g⁻¹ capacity fading), showing that the PIM-1 framework does retard the shuttling effective at low rate conditions. Furthermore, the capacity remained above 600 mA h g⁻¹ for PEO-PIM-8% at a high rate of 2C, while PEO only delivers 366 mA h g⁻¹. The corresponding voltage profiles are presented in Figure 5b,c. Next, the cycle life of the PEO-PIM-8% and PEO cells at 0.5C rate is compared in Figure 5d,e. The cell with PEO-PIM-8% electrolyte

exhibits an initial capacity of 1181 mA h g⁻¹, which outperforms that with PEO (928 mA h g⁻¹). In addition, the capacity of PEO dropped dramatically below 500 mA h g⁻¹ after only 26 cycles. Whereas, PEO-PIM (8%) maintained a capacity over 890 mA h g⁻¹ after 50 cycles and 730 mA h g⁻¹ after 100 cycles, indicating much a more stable cycling performance. Moreover, a high Coulombic efficiency over 98% can be retained in the cell using PEO-PIM-8%, which is much higher than those using PEO (less than 90% after 100 cycles). This is another evidence for suppressed shuttle effect with the introduction of PIM-1 framework. It is noteworthy that although PIM-1 has facilitated enhanced cycling performance, the shuttling issue in this system cannot be fully addressed by itself as polysulfide will diffuse along the percolating PEO domains and leads to inevitable capacity fading. In addition, cathode optimization, which is critical to electrochemical performance, should be implemented to jointly mitigate the loss of polysulfide.^[39–41]

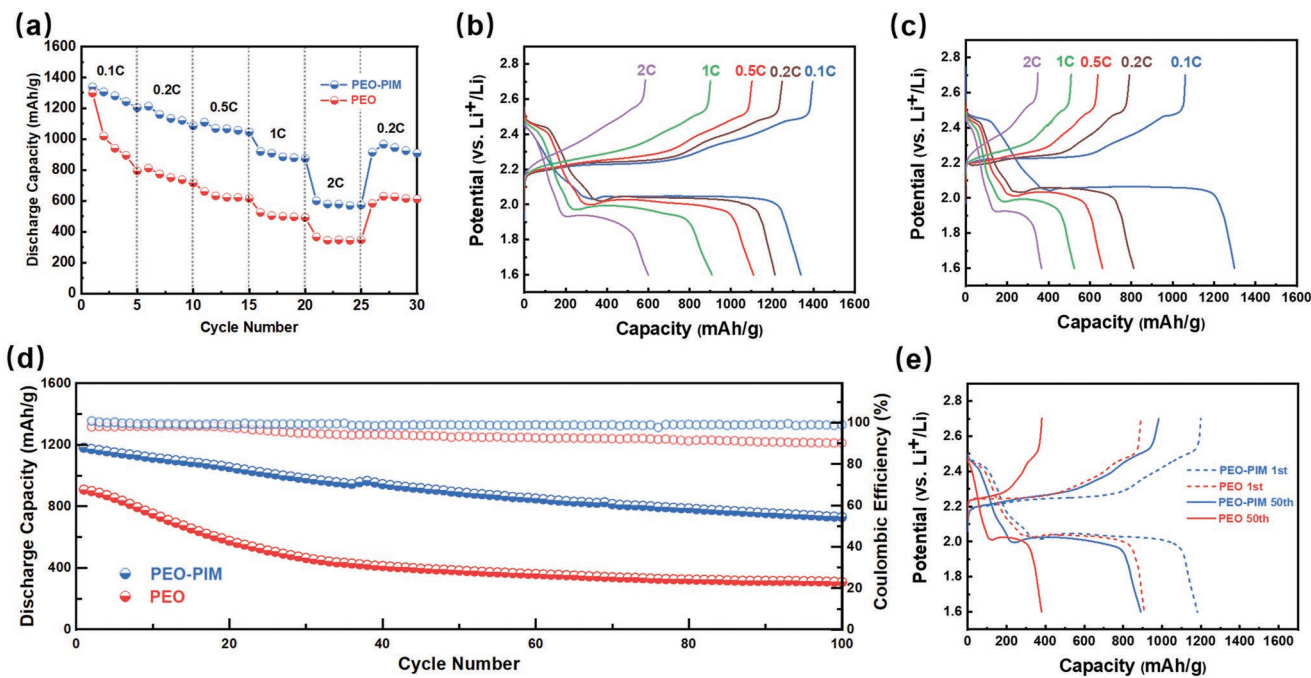


Figure 5. a) Rate discharge capacities of S@C/PEO-PIM/Li and S@C/PEO/Li at different rate. Charge–discharge profiles of b) S@C/PEO-PIM/Li and c) S@C/PEO/Li at different rate (0.1C, 0.2C, 0.5C, 1C, and 2C). d) Comparison of cycling performance of S@C/PEO-PIM/Li and S@C/PEO/Li under 0.5C. e) Charge–discharge profiles of S@C/PEO-PIM/Li and S@C/PEO/Li of 0.5C at 1st cycle and 50th cycle under 0.5C.

To further demonstrate the advantages offered by the PEO-PIM electrolyte in terms of flexibility and mechanical resilience, solid-state Li–S pouch cells (S@C/PEO-PIM/Li) were assembled and tested at 60 °C. Figure 4a shows that

the pouch cell works normally at 0.5C when folded to various angles, without short circuiting or losing capacity. Moreover, as shown in Figure 6b–d, the pouch cell can still provide a current even after significant abuse via cutting and nail

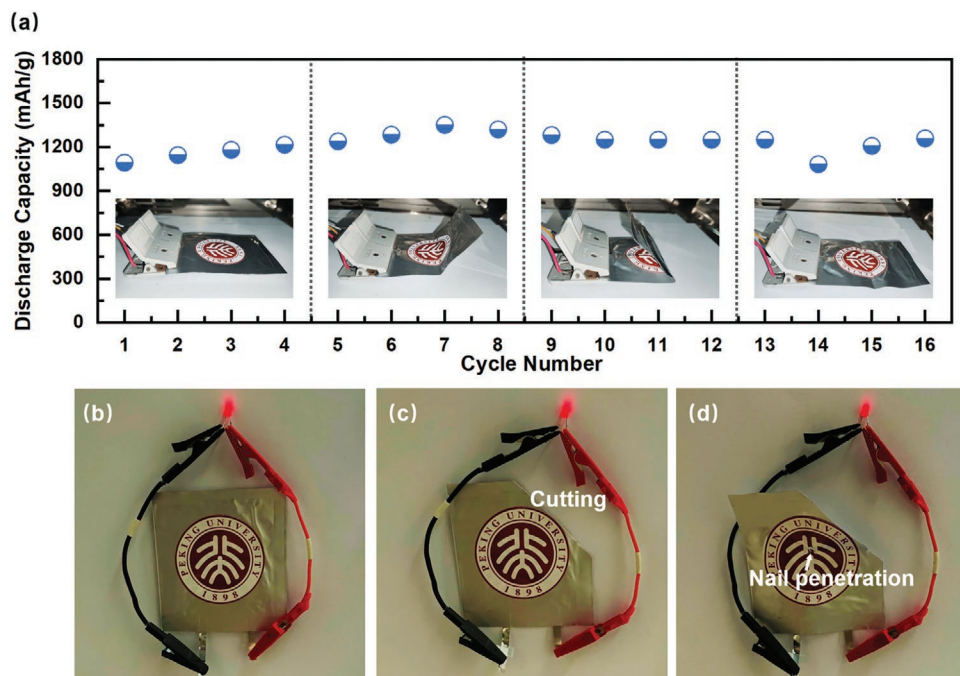


Figure 6. a) Cycling performance of the assembled S@C/PEO-PIM/Li pouch cell at different bending deformation degrees at 0.5C, 60 °C. b) Assembled S@C/PEO-PIM/Li pouch cell lighting a LED bulb, as well as after c) cutting and d) nail penetration.

penetration, demonstrating that PEO-PIM promises excellent safety performance, highlighting the exciting future prospects of solid-state Li–S batteries.

3. Conclusion

In summary, through employing PIM-1 as an organic framework for a PEO, a composite SPE with highly desirable properties for solid-state Li–S batteries has been manufactured. Exhibiting high rigidity and contorted spiro-centers, PIM-1 has effectively boosted the mechanical strength and hardness of the PEO electrolyte by an order of magnitude, while the ionic conductivity of the composite electrolyte has also been improved due to the lowered PEO crystallinity. As a result, better stability when utilized with metallic Li anodes, and lower overpotentials, could be achieved. Moreover, PIM-1 has been shown to trap polysulfide species, owing to its electrophilic functional groups, hence mitigating the shuttling effect. Finally, solid-state Li–S batteries using a PEO-PIM composite electrolyte has achieved greatly improved rate performance, cycling stability, and excellent safety features (see Table S3, Supporting Information, for detailed performance comparison with other reported works). By introducing one single component exhibiting desirable properties to tackle multiple issues in a system, this work has demonstrated a simple yet effective route to modify solid electrolytes without lengthy preparation as well as complex multicomponent systems, which promotes the widespread application of solid-state battery one step further.

4. Experimental Section

Materials and Chemicals: PEO (average Mw, 2 000 000), lithium bis(trifluoromethanesulfonyl)imide (LiTFSI), sublimed sulfur, anhydrous N,N-dimethylformamide (DMF), CH₃CN, and K₂CO₃ were purchased from Macklin. Carbon black (super P) and sulfur/carbon composite cathode material were supplied by Shenzhen Kejing Co., Ltd. 5,5',6,6'-tetrahydroxy-3,3,3',3'-tetramethylspirobisindane and 2,3,5,6-tetrafluoro-terephthalonitrile were purchased from Aladdin Chemical Co., Ltd.

Synthesis of PIM-1: 5,5',6,6'-tetrahydroxy-3,3,3',3'-tetramethylspirobisindane (10.25 g) and 2,3,5,6-tetrafluoro-terephthalonitrile (6.02 g) were mixed and dissolved in anhydrous DMF (200 mL). Anhydrous K₂CO₃ (33.34 g) powder was added to the mixture subsequently, and the temperature of mixture was stirred at 70 °C for 72 h with the atmosphere of argon. Then, the reaction was cooled down and poured into deionized water with stirring. The mixture was filtered and washed with deionized water thrice, and then dried to gain the yellow solid. The crude product was dissolved in tetrahydrofuran and precipitated by methyl alcohol in order to gain the PIM-1 final product.

Preparation of Solid Polymer Electrolytes: The dried PEO (Mw, 2 × 10⁶, 0.3 g) was mixed with LiTFSI (0.08 g) in 8 mL CH₃CN (AR grade), and the mixture was stirred at 70 °C for 12 h. The PIM-1 synthetic product was dissolved in trichloromethane (2 mL) and was stirred at 50 °C for 12 h. Various mass ratios of PIM-1 to PEO (0%, 4%, 8%, and 12%) were obtained by mixing the two solutions mentioned above. The new mixture colloidal was stirred at 50 °C for 12 h and casted onto the Teflon substrate in argon-filled glove box. The film was dried at room temperature, forming smooth and flat SPEs with the thickness of ≈50 μm.

Material Characterization: A Bruker D8 Advance X-ray diffraction analyzer (Cu Kα radiation, λ/4 0.154 nm) was applied to detect the crystal structure of the polymer electrolyte films. The morphology of

the electrolytes was characterized using a field-emission scanning electron microscope (SEM) (ZEISS Supra 55), with the voltage of 5.0 kV. The FT-IR spectra were obtained by a PerkinElmer Frontier FT-IR analyzer. Stress–strain curves were recorded using a MARK-10 ESM303 mechanical tester at a speed of 2.5 mm s⁻¹. Nano-indentation was tested via Agilent U9820A Nano Indenter G200. Thermogravimetric analysis (TGA) was measured by METTLER TOLEDO TGA/DSC1 system to detect the decomposition temperature of the polymer electrolytes. A Bruker Multimode 8 AFM was applied to test the surface morphology, modulus, and adhesion of polymer membranes.

Battery Assembly: Cathode electrodes were prepared by mixing the sublimed sulfur or S@C composite material, super P, and polyvinylidene fluoride in a weight ratio of 8:1:1. The N-methylpyrrolidone was used as the solvent and stirred to form a homogeneous slurry, which was subsequently coated onto an aluminum foil using a 300 μm height blade. The slurry was dried in a vacuum oven at 80 °C for 12 h and punched into 10 mm diameter plates. The active material loading of cathode electrode was around 1 mg cm⁻². Then, the newly punched electrodes were dried in a vacuum oven for 12 h and prepared to be assembled. 2025-type coin cells were assembled by fabricating stainless steel (SS)/SPE/SS, Li/SPE/SS, Li/SPE/Li and cathode electrodes (S/C and S)/SPE/Li in an argon-filled glove box.

Electrochemical Measurements: The galvanostatic discharge–charge tests of coin cells were applied by Neware battery cycler at 60 °C. The capacity and cycling stability measurements of S and S/C half cells were tested at different rate. Symmetrical Li cells with different ratio of PIM-1 were charged and discharged at the current was measured using a CHI 660E electrochemical workstation from open-circuit potential to 6 V to detect the electrochemical windows. EIS were tested by Solartron electrochemical workstation with a frequency range of 1 MHz–100 mHz to measure the ionic conductivities at different temperature.

Density Functional Theory Calculations: All calculations were based on the Gaussian 09 package by the DFT method. The authors used m062x/6-311G** theory level to optimize the molecular structure and calculate the adsorption binding energies. The split-valence-shell Gaussian basis set 6-311G** was used for the C, O, H, N, S, and Li atoms. Gauss View software was used to process the data and draw the structural diagram. The adsorption binding energy (ΔE_{bind}) was calculated to measure the binding strength of Li₂S_n (Li₂S₂, Li₂S₄, Li₂S₆, and Li₂S₈) species and the polymer X (PEO/PIM-1). It was defined by

$$\Delta E_{bind} = E_{\text{Li}_2\text{S}_n+\text{X}} - E_{\text{Li}_2\text{S}_n} - E_{\text{X}} + E_{\text{BSSE}} \quad (1)$$

where $E_{\text{Li}_2\text{S}_n+\text{X}}$ denoted the total energy of the Li₂S_n/X adsorbed system; the $E_{\text{Li}_2\text{S}_n}$ and E_{X} were the energies of isolated Li₂S_n species and PEO(PIM-1) calculated at their states. The last term E_{BSSE} was the energy of the basis set superposition error (BSSE) which was obtained by using the counterpoise method.

Supporting Information

Supporting Information is available from the Wiley Online Library or from the author.

Acknowledgements

Y.J., K.Y., M.L., and S.C. contributed equally to this work. This research was financially supported by National Key R&D Program of China (2016YFB0700600), National Key R&D Program of China (2016YFB0100300), the Shenzhen Science and Technology Research Grant (JCYJ20200109140416788), the Chemistry and Chemical Engineering Guangdong Laboratory (Grant No. 19220180), and National Key R&D Program of China (2020YFB07045000). T.S.M. thanks the Faraday Institution (EP/S003053/1) for support via the LiSTAR project (FIRG014).

Conflict of Interest

The authors declare no conflict of interest.

Data Availability Statement

Research data are not shared.

Keywords

ion conductance, intrinsic microporosity, mechanical properties, poly(ethylene oxide) electrolytes, polymers, polysulfide shuttling

Received: May 21, 2021

Revised: July 7, 2021

Published online: August 26, 2021

- [1] J. Zheng, Y. Ye, F. Pan, *Natl. Sci. Rev.* **2020**, *7*, 242.
- [2] S. Yang, R. He, Z. Zhang, Y. Cao, X. Gao, X. Liu, *Matter* **2020**, *3*, 27.
- [3] L. Yang, K. Yang, J. Zheng, K. Xu, K. Amine, F. Pan, *Chem. Soc. Rev.* **2020**, *49*, 4667.
- [4] M. Jana, R. Xu, X.-B. Cheng, J. S. Yeon, J. M. Park, J.-Q. Huang, Q. Zhang, H. S. Park, *Energy Environ. Sci.* **2020**, *13*, 1049.
- [5] W. J. Chen, B. Q. Li, C. X. Zhao, M. Zhao, T. Q. Yuan, R. C. Sun, J. Q. Huang, Q. Zhang, *Angew. Chem., Int. Ed.* **2020**, *59*, 10732.
- [6] S. H. Kim, J. H. Kim, S. J. Cho, S. Y. Lee, *Adv. Energy Mater.* **2019**, *9*, 1901841.
- [7] M. Li, J. E. Frerichs, M. Kolek, W. Sun, D. Zhou, C. J. Huang, B. J. Hwang, M. R. Hansen, M. Winter, P. Bieker, *Adv. Funct. Mater.* **2020**, *30*, 1910123.
- [8] Y.-X. Song, Y. Shi, J. Wan, S.-Y. Lang, X.-C. Hu, H.-J. Yan, B. Liu, Y.-G. Guo, R. Wen, L.-J. Wan, *Energy Environ. Sci.* **2019**, *12*, 2496.
- [9] J. Xiang, L. Yang, L. Yuan, K. Yuan, Y. Zhang, Y. Huang, J. Lin, F. Pan, Y. Huang, *Joule* **2019**, *3*, 2334.
- [10] M.-c. Pang, K. Yang, R. Brugge, T. Zhang, X. Liu, F. Pan, S. Yang, A. Aguadero, B. Wu, M. Marinescu, H. Wang, G. J. Offer, *Mater. Today* **2021**, <https://doi.org/10.1016/j.mattod.2021.02.011>.
- [11] X. Yang, M. Jiang, X. Gao, D. Bao, Q. Sun, N. Holmes, H. Duan, S. Mukherjee, K. Adair, C. Zhao, J. Liang, W. Li, J. Li, Y. Liu, H. Huang, L. Zhang, S. Lu, Q. Lu, R. Li, C. V. Singh, X. Sun, *Energy Environ. Sci.* **2020**, *13*, 1318.
- [12] Z. Wang, L. Yang, J. Liu, Y. Song, Q. Zhao, K. Yang, F. Pan, *ACS Appl. Mater. Interfaces* **2020**, *12*, 48677.
- [13] Z. Xue, D. He, X. Xie, *J. Mater. Chem. A* **2015**, *3*, 19218.
- [14] M. Yan, J. Y. Liang, T. T. Zuo, Y. X. Yin, S. Xin, S. J. Tan, Y. G. Guo, L. J. Wan, *Adv. Funct. Mater.* **2019**, *30*, 1908047.
- [15] R. Fang, H. Xu, B. Xu, X. Li, Y. Li, J. B. Goodenough, *Adv. Funct. Mater.* **2020**, *31*, 2001812.
- [16] B. K. Money, J. Swenson, *Macromolecules* **2013**, *46*, 6949.
- [17] L. Yang, Z. Wang, Y. Feng, R. Tan, Y. Zuo, R. Gao, Y. Zhao, L. Han, Z. Wang, F. Pan, *Adv. Energy Mater.* **2017**, *7*, 1701437.
- [18] H. Zhang, U. Oteo, X. Judez, G. G. Eshetu, M. Martinez-Ibañez, J. Carrasco, C. Li, M. Armand, *Joule* **2019**, *3*, 1689.
- [19] G. G. Eshetu, X. Judez, C. Li, M. Martinez-Ibañez, I. Gracia, O. Bondarchuk, J. Carrasco, L. M. Rodriguez-Martinez, H. Zhang, M. Armand, *J. Am. Chem. Soc.* **2018**, *140*, 9921.
- [20] C. Wang, T. Wang, L. Wang, Z. Hu, Z. Cui, J. Li, S. Dong, X. Zhou, G. Cui, *Adv. Sci.* **2019**, *6*, 1901036.
- [21] R. Tan, J. Yang, J. Zheng, K. Wang, L. Lin, S. Ji, J. Liu, F. Pan, *Nano Energy* **2015**, *16*, 112.
- [22] N. Wu, P. H. Chien, Y. Qian, Y. Li, H. Xu, N. S. Grundish, B. Xu, H. Jin, Y. Y. Hu, G. Yu, J. B. Goodenough, *Angew. Chem., Int. Ed.* **2020**, *59*, 4131.
- [23] J. Wan, J. Xie, X. Kong, Z. Liu, K. Liu, F. Shi, A. Pei, H. Chen, W. Chen, J. Chen, X. Zhang, L. Zong, J. Wang, L. Q. Chen, J. Qin, Y. Cui, *Nat. Nanotechnol.* **2019**, *14*, 705.
- [24] P. Zhai, N. Peng, Z. Sun, W. Wu, W. Kou, G. Cui, K. Zhao, J. Wang, *J. Mater. Chem. A* **2020**, *8*, 23344.
- [25] H. Wu, Y. Xu, X. Ren, B. Liu, M. H. Engelhard, M. S. Ding, P. Z. El-Khoury, L. Zhang, Q. Li, K. Xu, C. Wang, J. G. Zhang, W. Xu, *Adv. Energy Mater.* **2019**, *9*, 1902108.
- [26] S. E. Doris, A. L. Ward, P. D. Frischmann, L. Li, B. A. Helms, *J. Mater. Chem. A* **2016**, *4*, 16946.
- [27] G. Genduso, Y. Wang, B. S. Ghanem, I. Pinna, *J. Membr. Sci.* **2019**, *584*, 100.
- [28] X. Wu, Z. Tian, S. Wang, D. Peng, L. Yang, Y. Wu, Q. Xin, H. Wu, Z. Jiang, *J. Membr. Sci.* **2017**, *528*, 273.
- [29] H. Zhao, Q. Xie, X. Ding, J. Chen, M. Hua, X. Tan, Y. Zhang, *J. Membr. Sci.* **2016**, *514*, 305.
- [30] B. K. Gupta, G. Kedawat, P. Kumar, M. A. Rafiee, P. Tyagi, R. Srivastava, P. M. Ajayan, *J. Mater. Chem. C* **2015**, *3*, 2568.
- [31] P. M. Budd, B. S. Ghanem, S. Makhseed, N. B. McKeown, K. J. Msayib, C. E. Tattershall, *Chem. Commun.* **2004**, 230.
- [32] H. L. Guo, H. Sun, Z. L. Jiang, J. Y. Hu, C. S. Luo, M. Y. Gao, J. Y. Cheng, W. K. Shi, H. J. Zhou, S. G. Sun, *ACS Appl. Mater. Interfaces* **2019**, *11*, 46783.
- [33] L. Liu, J. Lyu, J. Mo, H. Yan, L. Xu, P. Peng, J. Li, B. Jiang, L. Chu, M. Li, *Nano Energy* **2020**, *69*, 10349.
- [34] L. L. Jia, Y. C. Ji, K. Yang, Z. J. Wang, H. B. Chen, F. Pan, *Chin. J. Struct. Chem.* **2020**, *39*, 200.
- [35] M. B. Dixit, W. Zaman, N. Hortance, S. Vujic, B. Harkey, F. Shen, W.-Y. Tsai, V. De Andrade, X. C. Chen, N. Balke, K. B. Hatzell, *Joule* **2020**, *4*, 207.
- [36] H. Qin, K. Fu, Y. Zhang, Y. Ye, M. Song, Y. Kuang, S.-H. Jang, F. Jiang, L. Cui, *Energy Storage Mater.* **2020**, *28*, 293.
- [37] Y. Song, L. Yang, L. Tao, Q. Zhao, Z. Wang, Y. Cui, H. Liu, Y. Lin, F. Pan, *J. Mater. Chem. A* **2019**, *7*, 22898.
- [38] J. W. Jeon, D. M. Kim, J. Lee, J. C. Lee, Y. S. Kim, K. T. Lee, B. G. Kim, *J. Mater. Chem. A* **2020**, *8*, 3580.
- [39] Y. Yao, H. Wang, H. Yang, S. Zeng, R. Xu, F. Liu, P. Shi, Y. Feng, K. Wang, W. Yang, X. Wu, W. Luo, Y. Yu, *Adv. Mater.* **2020**, *32*, 1905658.
- [40] R. Wang, J. Yang, X. Chen, Y. Zhao, W. Zhao, G. Qian, S. Li, Y. Xiao, H. Chen, Y. Ye, G. Zhou, F. Pan, *Adv. Energy Mater.* **2020**, *10*, 1903550.
- [41] Y. Wang, Y. Yu, Y. Tan, T. Li, Y. Chen, S. Wang, K. Sui, H. Zhang, Y. Luo, X. Li, *Adv. Energy Mater.* **2019**, *10*, 1903233.